Ultramicroscopy 171 (2016) 177–185

Contents lists available at ScienceDirect

Ultramicroscopy

journal homepage: www.elsevier.com/locate/ultramic

EBSD spatial resolution for detecting sigma phase in steels

S. Fernandez Bordín [a], S. Limandri [a], J.M. Ranalli [b], G. Castellano [a,*]

[a] Instituto de Física Enrique Gaviola, CONICET. M. Allende s/n, Ciudad Universitaria, 5000 Córdoba, Argentina
[b] Comisión Nacional de Energía Atómica, Av. Gral. Paz 1499, San Martín, 1650 Buenos Aires, Argentina

ARTICLE INFO

Article history:
Received 4 April 2016
Received in revised form
2 September 2016
Accepted 18 September 2016
Available online 20 September 2016

Keywords:
Electron backscatter diffraction
Spatial resolution
Sigma phase
Stainless steel
Monte Carlo simulation

ABSTRACT

The spatial resolution of the electron backscatter diffraction signal is explored by Monte Carlo simulation for the sigma phase in steel at a typical instrumental set-up. In order to estimate the active volume corresponding to the diffracted electrons, the fraction of the backscattered electrons contributing to the diffraction signal was inferred by extrapolating the Kikuchi pattern contrast measured by other authors, as a function of the diffracted electron energy. In the resulting estimation, the contribution of the intrinsic incident beam size and the software capability to deconvolve patterns were included.

A strong influence of the beam size on the lateral resolution was observed, resulting in 20 nm for the aperture considered. For longitudinal and depth directions the resolutions obtained were 75 nm and 16 nm, respectively. The reliability of this last result is discussed in terms of the survey of the last large-angle deflection undergone by the backscattered electrons involved in the diffraction process.

Bearing in mind the mean transversal resolution found, it was possible to detect small area grains of sigma phase by EBSD measurements, for a stabilized austenitic AISI 347 stainless steel under heat treatments, simulating post welding (40 h at 600 °C) and aging (284 h at 484 °C) effects—as usually occurring in nuclear reactor pressure vessels.

1. Introduction

The characterization of crystalline structures, as well as orientation, shape and phase distribution is important in materials science, since, for example, grain size is related with mechanical, physical and superficial material behaviour. Recent advances in electron backscatter diffraction (EBSD) in scanning electron microscopes have shown its potential to study individual grain orientation, local texture, etc. [1].

The spatial resolution in EBSD, *i.e.*, the resolution measured at the sample surface and along the depth direction, is a function of the backscattered electron yield, the incident electron beam size, current and energy, the interaction volume and the software used for indexing the diffraction patterns. Two types of spatial resolution are usually defined: the physical resolution, which represents the maximum distance to a high angle grain boundary for which the diffraction pattern acquired corresponds exclusively to one grain; and the effective resolution, that represents how precisely a high angle grain boundary can be resolved by using deconvolution algorithms. The effective resolution is, in general, better than the physical resolution [2].

Due to the high sample tilt (typically 70°), the beam profile on the sample is asymmetric (Fig. 1). For this reason, the resolution on the sample surface is characterized along two directions: perpendicular (longitudinal) and parallel (lateral) to the sample tilt axis. Calculations based on trigonometric relations estimate that the longitudinal resolution should be around 3 times higher than the lateral resolution for a 70° tilt angle [3,4].

According to the compilation of EBSD resolution data performed by Steinmetz and Zaefferer [5], the best effective spatial resolution reported until 2010 is 6–9 nm for Pt measured at 25 keV incident electron energy [6], whereas the best physical resolution is 90 and 35 nm for perpendicular and parallel tilt directions, respectively, for Fe measured at 15 keV [7]. In both cases the methodology followed to estimate the resolution consisted in performing a scanning through a known high angle grain boundary. Steinmetz and Zaefferer [5] improved the resolution by lowering the incident beam energy, obtaining 10 nm for steel (at 7.5 keV). The best resolution is nowadays obtained with FE-SEMs [4], due to their high probe currents and the small diameter of the incident electron beam.

A reasonable estimate for the spatial resolution must rely in an adequate model accounting for the energy range of the backscattered electrons (BE) contributing to the diffraction phenomenon. According to Ren *et al.* [8], BE with energies within 90% of the incident energy (E_o), called "low-loss electrons" are the main contributors to the diffraction signal; with this constraint, they performed Monte Carlo simulations, obtaining physical resolutions of 90 nm, 150 nm and 20 nm in lateral, longitudinal and depth

* Corresponding author.

http://dx.doi.org/10.1016/j.ultramic.2016.09.010
0304-3991/

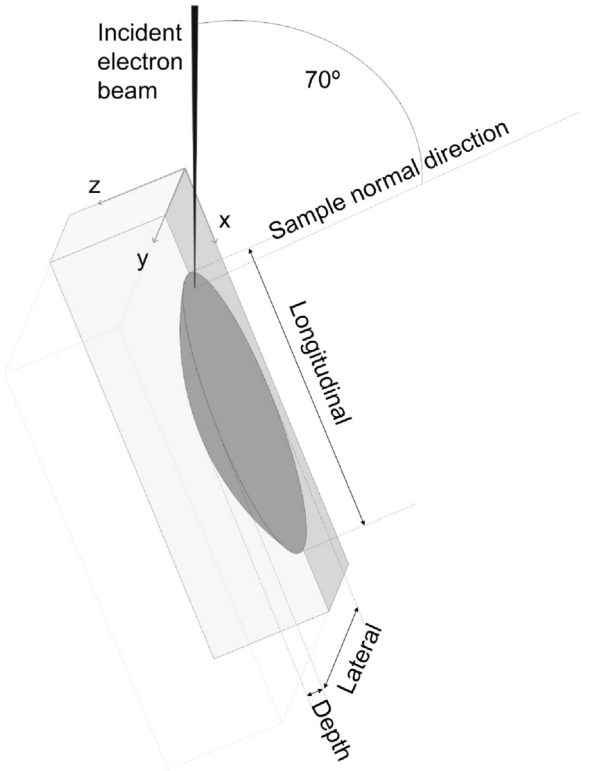

Fig. 1. Scheme of the interaction volume and the characteristic directions involved in the typical EBSD configuration.

directions, respectively, for Cu irradiated by a 20 keV electron beam.

Recently, Deal *et al.* [9] studied the dependence of the EBSD pattern quality on the energy of the BE for a wide atomic number range, by attaching to the EBSD detector an energy filter with a resolution better than 10 eV. They obtained a distribution of the BE contributing to diffraction as a function of their energy (for a 15 keV incident beam), which led them to conclude that the major contributors to the diffracted electron signal are electrons with around 97% of E_o. They also observed that the contribution of electrons within 90% of E_o is higher than that corresponding to 80% of E_o. Nevertheless, there is a small diffraction contribution from electrons well below E_o; this contribution, despite being small, preferentially enhances the diffuse background and not the EBSD pattern, with the consequent loss of resolution.

According to recent studies, electron collisions with nuclei at the atomic positions within the unit cell (with consequent nuclear recoil) constitute the mechanism which produces incoherent scattering events at fixed localization, enabling the formation of Kikuchi patterns [10]. These incoherently scattered electrons form internal point sources, and the subsequent interference along the outgoing trajectories results in a Kikuchi pattern [11]; inelastic events along the outgoing trajectory of the BE electrons will degrade the interference pattern formation [12]. For large angle deflections, the scattered electron transfers a significant amount of momentum to a single atom. Since the recoil energy depends on the target atom, the contribution of electrons scattered from different elements can be discriminated in an energy-filtered experiment [13,14]. The detailed element distribution in each crystallographic plane may therefore be inferred, which constitutes an attractive tool to investigate the crystallographic structure close to a material surface [11,15].

The spatial resolution is a measure of the minimum phase size detectable with the considered technique. It is very important to count with an estimate for this resolution when the goal is to determine the presence of minor phases. An interesting example is the characterization of stainless steels under different heat treatments, since for certain temperatures and aging times, the material behaviour may be affected by the appearance of secondary phases, such as the sigma-phase (σ-phase). The presence of the σ-phase affects not only corrosion properties but also reduces the material toughness [16].

In this work the EBSD spatial resolution for the detection of σ-phase in steels is studied by Monte Carlo simulations based on the PENELOPE routine package [17], which generates electron paths through contiguous free flights between successive interactions, and has successfully described electron transport phenomena in materials [18]. By incorporating the intrinsic incident beam size and the algorithm capability for pattern deconvolution, the effective spatial resolution is estimated. Based on the effective transversal mean resolution obtained here, a strategy for optimizing measurement times and map quality is proposed. In addition, the presence of this phase is studied for the particular case of an austenitic stainless steel AISI 347 under heat treatments representing post welding and aging conditions in nuclear reactors pressure vessels.

2. Monte Carlo simulations

Monte Carlo simulations were performed in order to investigate the interaction volume of the backscattered electrons contributing to the diffraction patterns in a steel sample. The example main program PENCYL distributed with the 2011 version of the PENELOPE routine package [17] was used for these simulations. Although this program is optimized for cylindrical geometries constituted by different layers, it was modified in order to register the spatial coordinates of the BE when they emerge from the sample, and also to accumulate the fraction of BE in a three-dimensional spatial grid. The diffraction pattern is considered to be originated in the last large-angle deflection event the outgoing electron undergoes, after which no incoherent scattering occurs.

It is worth noticing that the PENELOPE package does not involve the continuous slowing-down approximation (CSDA), as with this oversimplified approach no energy loss fluctuations are allowed, and unrealistic energy distributions of diffused monoenergetic electron beams are obtained [19,20]. On the contrary, electron paths are individually simulated by means of contiguous free flights between successive interactions, each interaction involving a stochastic energy loss, assessed by means of the corresponding cross sections (total and differential) [21].

A homogeneous material with cylindrical geometry, 1.5 μm radius and 2.5 μm thickness with FeCr stoichiometric formula (corresponding to the σ-phase) was used. The simulations were performed for a point source parallel electron beam, with 20 keV incident energy and 70° sample tilt angle. In the simulations, electrons leaving the sample surface with energies above a cutoff energy E_c are recorded in order to generate the spatial distributions sought. The number of primary electrons was 1×10^9 for each run, and a total of 13 runs were performed for each set of simulations corresponding to different cutoff energies: 0.3, 12, 13.3, 14.7, 16.0, 16.7, 17.3, 18.0, 18.7, 19.0, 19.6, 19.7, and 19.8 keV.

A first set of simulations was performed in order to study the resolution in longitudinal and lateral directions (see Fig. 1). The three-dimensional grid used corresponds to $601 \times 601 \times 1$ voxels of 5 nm × 5 nm × 1.5 μm. The second set was used to determine the depth resolution. In this case the spatial grid in which the BE were counted corresponds to 60 slices of 1.5 μm × 1.5 μm × 1 nm.

3. Experimental

Austenitic steel weld deposits on carbon or low alloy steels are widely used for building pressure vessels with the aim of protecting the base material from corrosion. In the particular case of nuclear industry, the cladding of reactor pressure vessels plays an additional role: avoiding metal base corrosion reduces the ion transport that can be activated when crossing the reactor nucleus, and consequently lowers the collective installation dose. In their formulation, a balance between different alloying elements is performed to obtain a ferrite content of 5–10%. This phase is unstable at the temperature used for the post welding heat treatment and can be decomposed in several minor phases. One of these is the σ-phase, the amount of which affects not only corrosion properties but also reduces the material toughness [16]. For this reason, the detection and study of precipitation mechanisms and the subsequent evolution of this phase during service is crucial.

The sample studied in this work corresponds to an AISI 347 austenitic stainless steel with nominal composition (in wt%) C: 0.03–0.04, Mn: 0.97–1.00, P: 0.017, S: 0.006, Si: 0.94, Cr: 18.9–19.0, Ni: 11.2–11.3, Ti: 0.012, Nb: 0.567–0.57, Co: 0.03, N: 0.021–0.023, rest Fe. Two heat treatments were applied to this sample: 40 h at 600 °C and 284.4 h at 452 °C. The first treatment corresponds to the post welding heat treatment, whereas the second one simulates operation conditions in nuclear reactor vessels for 30 years at 300 °C.

The sample was included in conductive resin, polished with 1200 μm paper, 9 μm, 6 μm, 3 μm and 1 μm diamond pastes, and colloidal silica (0.05 μm) during 1, 5, 4, 4, 3 and 10 min with a velocity of 180, 150, 150, 150, 150 and 120 rpm, respectively. In all cases the force applied was 18 N.

Measurements were carried out in a scanning electron microscope FE-SEM Σigma- Carl Zeiss with a Schottky electron gun. The electron backscatter detector is an Oxford Nordlys Nano with a CCD camera with 1344 × 1024 pixels and a 40 mm × 35 mm front phosphor screen. An SDD X-ray detector is also attached to the SEM with an 80 mm^2 front area and a nominal resolution of 127 eV for Mn-Kα line (5.893 keV). The AZtec 3.1 software (Oxford Instruments) was used for phase indexing and deconvolution. In this software, the band positions are identified via Hough transform, and the angles between bands are calculated and compared with a list of interplanar angles for the analysed structures. A method called class indexing examines permutations of four bands, and the basis of indexing lies in the agreement or disagreement between the measured bands and the reference crystal reflectors.

The main purpose of this work was to search and identify a minor secondary phase; it was therefore important to optimize the microscope parameters in order to achieve fast measurements which allowed to scan large areas in a reasonable time (at the expense of worsening spatial resolution). The following SEM parameters were thus chosen: 20 keV incident energy, 120 μm aperture, 8.5 mm working distance, 70° tilt angle, and 4 nA beam current. A 4 × 4 binning and 15 ms exposure time per frame were used for the CCD camera. For the acquisition of 1500X maps, 0.1 μm and 0.2 μm step sizes were chosen, whereas high magnification maps (3000X) were recorded with 0.05 μm steps.

In order to estimate the intrinsic incident beam size, secondary electron images were acquired for a Ni grid with sharp edges. Intensity profiles were repeatedly obtained along straight lines perpendicular to the border of this Ni grid, for the 120 μm aperture used in this work, and also for the minimum aperture available (7.5 μm) with a scanning pixel size of 1.73 nm.

4. Results and discussion

4.1. Lateral and longitudinal resolution

The initial study of the present work involved the dependence of the backscattered electron fraction η with the cutoff energy E_c. As can be observed in Fig. 2, η slowly decreases for E_c between 0.3 and 16 keV whereas the decreasing rate is higher for larger E_c values. 45% of the BE have energies in the range from 18 to 20 keV, which is in agreement with the results obtained in [8], and only 18% bear energies within 97% of the incident energy. Spatial distributions for backscattered electrons were obtained for different E_c values. Fig. 3 shows the resulting distributions for E_c=0.3 keV and E_c=19 keV; as expected, the distribution is symmetric in lateral direction, whereas it is elongated in longitudinal direction.

The transversal shape and size of the interaction volume can be characterized by the widths along lateral (L_y) and longitudinal (L_x) directions (see Fig. 1). As in the case of the 68% percentage contained within ± one standard deviation for a Gaussian distribution, these widths were defined as those integrating a 0.68 fraction of the BE distribution. When E_c increases, the interaction volume decreases acquiring an elongated shape in the longitudinal direction (Fig. 4). According to Humphreys et al. [4], L_x should be 3 times higher than L_y; this occurs for BE with energies within 97.5% of the incident energy.

As mentioned in Section 1, Deal et al. [9] studied the contribution of BE to the diffraction patterns as a function of their energy for Si, Ir and Fe samples irradiated at 15 keV by using energy filters between the sample and the EBSD detector. They observed that the main contribution to the diffraction pattern is due to electrons undergoing low energy losses (less than 20%), and the maximum pattern contrast is given for electrons with energies within 97% of the incident energy. Based on this study and translating this trend to a 20 keV incident beam, i.e., assuming the same dependence of the pattern contrast on the cutoff energy, the relative fractions of BE contributions to the diffraction signal as a function of E_c have been obtained (Table 1). The backscattered electron volume contributing to the diffraction signal, hereinafter diffraction volume, was thus obtained by the following equation:

$$v_{ijk} = \sum_{E_c} \eta_{v_{ijk},E_c} A_{E_c} \quad (1)$$

where v_{ijk} is the *ijk*-voxel of the diffraction volume, η_{v_{ijk}, E_c} is the fraction of BE in voxel *ijk* for the cutoff energy E_c, and A_{E_c} is the relative contribution factor given in Table 1. The spatial distribution corresponding to the diffracted electrons is shown in Fig. 3c. The corresponding lateral and longitudinal widths are 145 nm and

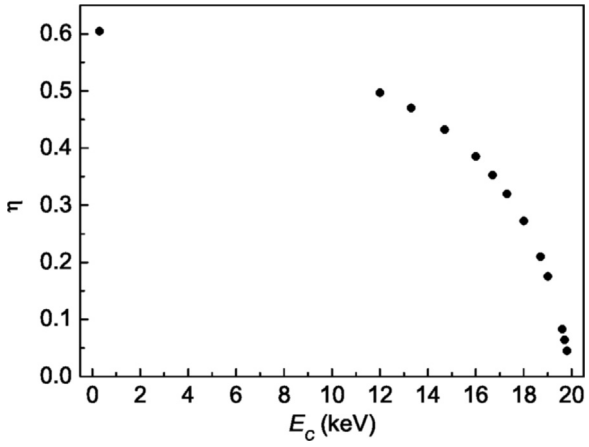

Fig. 2. Backscattered electron coefficient η as a function of the cutoff energy (E_c).

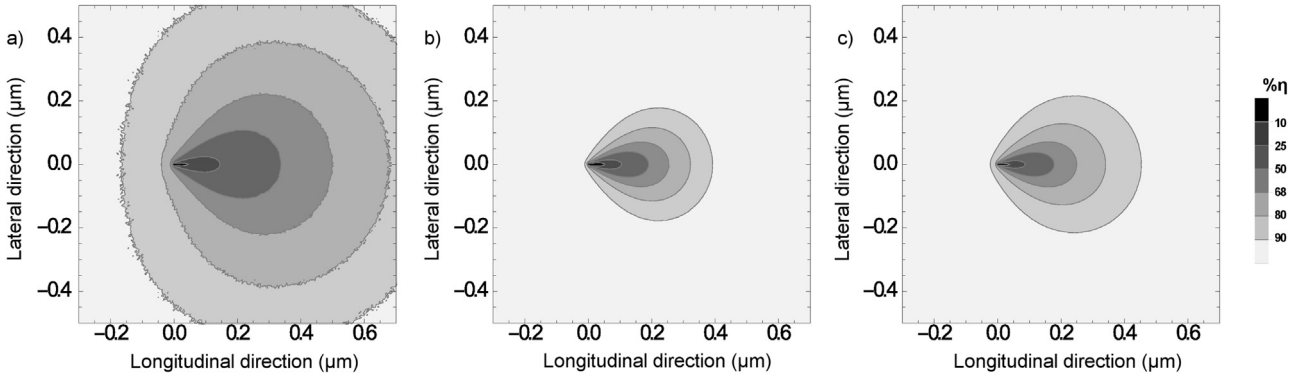

Fig. 3. BE spatial distribution for (a) E_c=0.3 keV and (b) E_c=18 keV. (c) Spatial distribution of BE contributing to the diffraction signal obtained by Eq. (1) – see text.

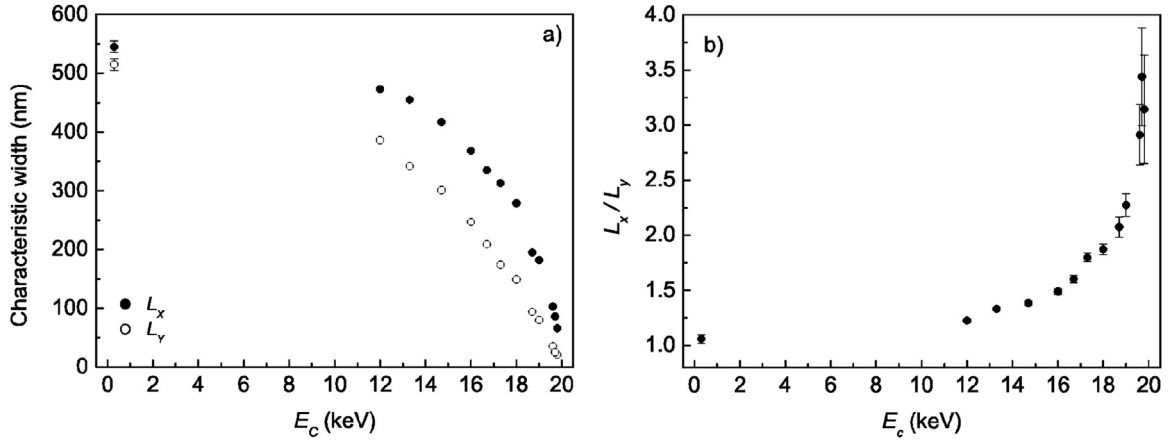

Fig. 4. Longitudinal (L_x) and lateral (L_y) widths (a) and aspect ratio (b) of the backscattering electron signal as a function of the cutoff energy.

Table 1
Relative contribution factors of BE to the diffraction volume.

E_c (keV)	A_{E_c}
12	0.010
13.3	0.021
14.7	0.035
16	0.062
16.7	0.075
17.3	0.091
18	0.122
18.7	0.15
19	0.167
19.6	0.151
19.7	0.103
19.8	0.014

256 nm, respectively, whereas its depth is 19 nm.

To estimate the effective resolution, the software ability to deconvolve overlapped patterns must be taken into account. It was assumed that: (1) the software correctly indexes a pattern corresponding to a grain when the signal coming from this grain represents at least 60% of the total signal, and (2) the diffraction signal is proportional to the number of electrons backscattered from the diffraction volume containing the corresponding grain. A similar approach was recently suggested by Tong et al. [22] in order to analyse the accuracy of cross correlation results of strain measurements; in their work, a more restrictive pattern mixing of 70%/30% was inferred, since only subtle differences are associated with elastic strains and rotations. Under these assumptions, the lateral/longitudinal effective resolution can be estimated by calculating the fraction of diffracted BE from a grain as a function of the distance to the interface (see Fig. 5). It can be seen that the diffraction signal is symmetric for the lateral resolution, whereas it bears a clear asymmetry for the longitudinal direction due to the non-normal beam incidence. The lateral and longitudinal resolutions obtained are 10 nm and 56 nm, respectively for a point source parallel electron beam. It is worth mentioning that these values are representative for resolutions associated to high-angle grain boundaries. On the contrary, special care must be taken when analysing residual strains by small local low-angle misorientations, where intrinsic sample features and software algorithm limitations may hinder the proper deconvolution and, therefore, the phase orientation determination [23].

For EBSD measurements, the larger apertures (wider spot sizes) are commonly used to get high currents, and hence to decrease acquisition times. Since larger apertures are related with important spherical and chromatic aberrations [24], the beam size can be above 100 times larger for these apertures than for smaller ones. In addition, the incident beam size depends on other SEM parameters, such as the gun type and the incident beam energy. In the case of field emission guns, the beam size varies from 0.1 nm to several tens of nm. For this reason, the incident beam size is a parameter that must be taken into account for a more realistic estimation of the resolution. The beam size is not provided by the manufacturer, so a methodology to infer this parameter is necessary. In this work the method proposed by Goldenshtein et al. [25] was followed to estimate the incident beam size. Intensity profiles were extracted from secondary electron images corresponding to a Ni grid, acquired at 20 keV with the smallest (7.5 μm) and largest (120 μm) apertures. Since the beam size for the smallest aperture is a few tenths of nm, the intensity profiles measured with this

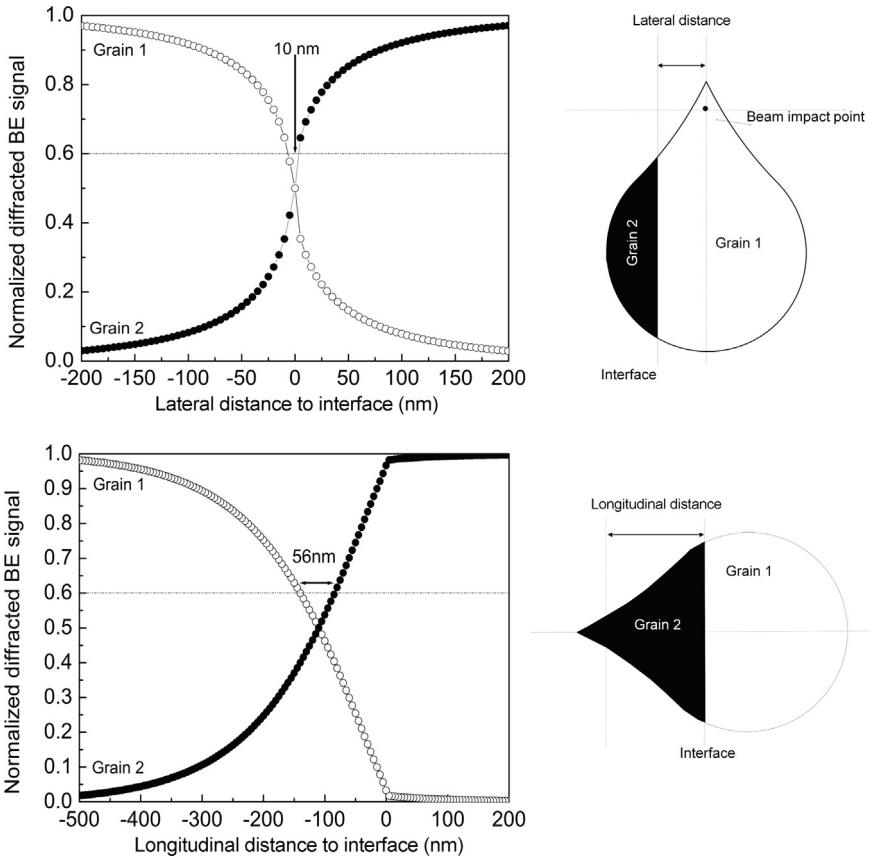

Fig. 5. Normalized diffraction BE signal as a function of (a) lateral and (b) longitudinal distance to the interface of two grains. Schematic diagrams representing both cases are shown beside the corresponding graphs.

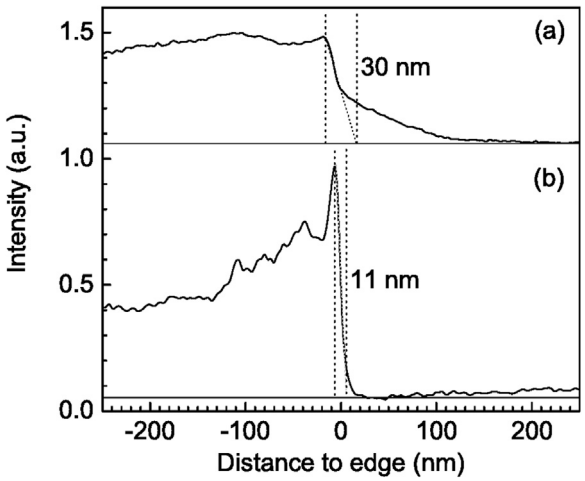

Fig. 6. Intensity profiles corresponding to secondary electron images of a Ni grid edge acquired at 20 keV with 7.5 μm (a) and 120 μm (b) apertures.

aperture can be associated with the interface morphology, whereas, for the larger aperture, the profiles are convolutions of the interface morphology and the beam profile (see Fig. 6). It can be seen that the profiles taken with the largest aperture rapidly decrease as the beam passes from the Ni region to the hollow area, displaying a slower decay when moving away from the interface. For the present study, the edge was defined through the first decay, since the second one corresponds to secondary detection artifacts [26]. The beam size was then assessed by subtracting the profiles corresponding to the two apertures (after averaging all the experimental determinations), obtaining a value of (17 ± 5) nm for the 120 μm aperture.

The beam size must be added in quadrature with the estimates furnished by the Monte Carlo simulations to obtain the lateral resolution, which therefore resulted 20 nm. For the longitudinal resolution, the quadrature sum involves the Monte Carlo result and the beam size multiplied by cosec(20°), which gave a final longitudinal resolution of 75 nm. The ratio longitudinal/lateral resolution is 3.75, which is close to the ratio predicted by Humphreys et al. [4]. It is thus important to notice that the intrinsic beam size is a determinant factor affecting the EBSD resolution, particularly along the lateral direction.

Spatial resolution may also be affected by the incident beam divergence. According to Reimer [26], a diaphragm of 120 μm in diameter in the objective lens, as the one used here, produces a beam angular aperture of around 10 mrad. In order to investigate the influence of this beam divergence in the transversal resolution, Monte Carlo simulations were carried out for apertures up to 50 mrad for an 18 keV cutoff energy, without altering the longitudinal and lateral widths of the distributions (less than 1%).

It is worth mentioning that, when estimating the effective spatial resolution, the influence of the detector resolution has not been taken into account. The conventional detector used here involves a phosphor front screen with a CCD camera, which may worsen the effective resolution in the acquisition process. In the measurements carried out in this work, however, the CCD camera binning set as the standard condition to achieve good resolution maps in reasonable times, makes this contribution negligible. In order to provide a quantitative estimate of this contribution, the use of a digital complementary metal-oxide semiconductor (CMOS) hybrid-pixel detector is necessary [27], which is out of the scope of the present investigation.

Although in general, experimental resolutions higher than

100 nm are achieved using microscopes with tungsten filaments, the results obtained here are in good agreement with the experimental resolutions reported by other authors by means of FEG microscopes (see, e.g., Table 1 in ref [5]).

4.2. Depth resolution

Depth-resolved dynamical EBSD simulations for Mo at 20 keV predict that the main contribution to the diffraction pattern takes place at a 10 nm depth, assuming an analytical depth distribution based on the maximum penetration attained by BE within 8% of the incident energy, obtained from Monte Carlo simulations (based on continuous slowing down approximation) [12]. A similar approach for 30 keV electrons on Si at 80° incidence angle show that electrons emerging from up to 7.5 nm are the main contributors to the diffraction pattern, for a Poisson depth distribution of scattering events [28].

The diffracting BE depth distribution may strongly differ from the maximum BE penetration distribution, since the outgoing electrons may undergo additional scattering events and consequently lose coherence. The Monte Carlo simulations carried out in this work survey the spatial coordinates where the BE last large-angle deflection occurs, assuming a 20° cutoff scattering angle; the corresponding diffraction process therefore originates from this position. The resulting depth distributions appear to be sensitive to this restriction, as shown in Fig. 7a for the σ-phase at E_c=18 keV; similar values were obtained for a 15° cutoff angle.

According to the present simulations, the depth encompassing 68% of the diffracting backscattered electrons varies from 30 nm to 7 nm for energies in the considered E_c range (Fig. 7b). The resulting depth resolution obtained from the diffraction volume – Eq. (1) – is therefore 16 nm. Data available in the literature about EBSD depth resolution is very scarce. Chen et al. [2] estimated the depth resolution with two different methods. The first one consisted in determining the minimum thickness of an amorphous layer necessary to completely loose the diffraction signal from a crystalline sample, obtaining a resolution of 4 nm for 20 keV electrons in a Cu sample. Zaefferer [7] obtained a depth resolution of 5.5–8 nm for Cr by applying the same strategy. These values provide lower bounds for the depth resolution, since once the amorphous material has been crossed, the electrons must also traverse at least a quarter of the corresponding extinction distance so that the diffraction takes place in the crystalline material [9,28].

The other method applied by Chen et al. [2] involves EBSD pattern measurements in a region close to a grain boundary for a bicrystalline sample. In this case, they obtained a depth resolution of 60 nm, which is 15 times higher than the one estimated with the first method. According to these authors, this difference is due to channeling effects, not taken into account in the first method applied (amorphous materials do not produce channeling). Specialized works in electron channeling state that the penetration depth related with this effect can be higher than 50 nm in Si [29] and 60–80 nm in steel [30], which implies that if this effect is important, it will strongly worsen the depth resolution attainable.

4.3. σ-phase characterization in an austenitic steel sample

Although data available in the literature for the σ-phase in AISI 347 stainless steel under heat treatments correspond to aging times higher than 100 h, an extrapolation seems to indicate that this phase should not be present for the aging times and temperatures used in this work. According to Schwind et al. [31], for this type of steel and for a heat treatment at 600 °C during 50,000 h, only 0.02% (in volume) of σ-phase was found. The study performed by Minami *et al.* [32] by optical microscopy, X-ray diffraction and transmission electron microscopy, shows that, at 600 °C, the σ-phase precipitates for times larger than 4000 h, whereas for 700 °C the time reduces to 1000 h. Gharehbaghi [33] observed this phase in a steel of similar composition for treatments at 700 and 800 °C during 500 h. Bearing in mind that the σ-phase precipitation is usually a very slow process occurring in long term agings, if present on the sample studied in this work, it is expectable to be found as small grains and in very low proportions. This is one of the reasons why it is important to know the resolution of the technique used to perform the sample characterization.

The possible growing areas corresponding to the σ-phase have been reported by several authors. These regions depend on the steel type and the heat treatment applied. Barcik [34] and Villanueva et al. [35] showed that σ-phase precipitates in triple points associated to ferrite, incoherent grain boundaries, and around grain inclusions. The precipitation can also occur at the ferrite-austenite interphase [36,37] and within the austenite grains if the aging time and temperature are high enough [38]. In some cases, the σ-phase was observed close to chromium and niobium carbides. Singhal [39] and Barcik [34] explained this growth occurs at expenses of chromium carbide. All the regions abovementioned are potential sites to search for the σ-phase on the studied sample.

Crystallographic data given by Yakel [40] were used to identify the σ-phase in EBSD patterns. This phase is represented as an

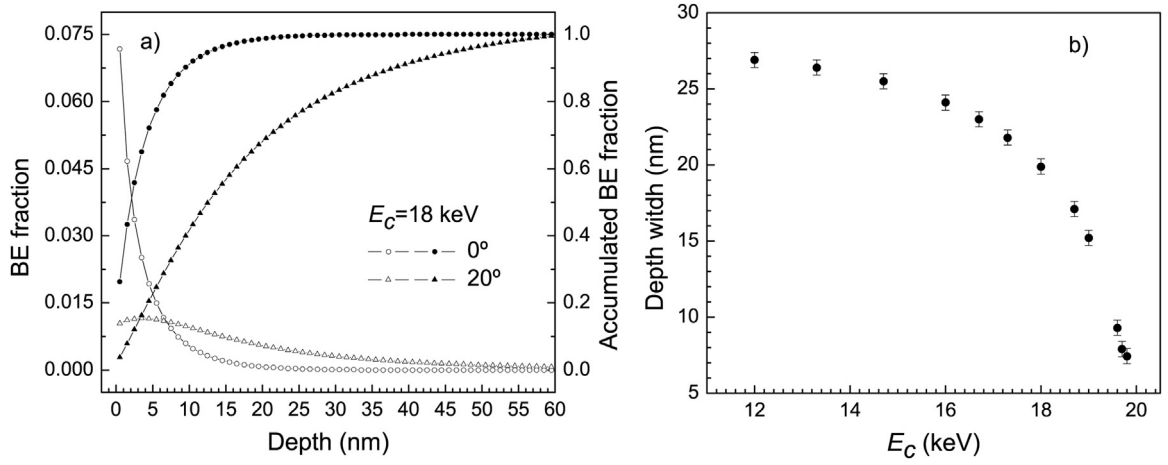

Fig. 7. (a) Backscattered electron depth distribution (hollow symbols) and accumulated depth distribution (full symbols) with E_c=18 keV, taking into account the last scattering event. Circles: any deflection; triangles: deflection higher than 20° (see text). (b) Depth widths for the backscattering electron signal as a function of the cutoff energy.

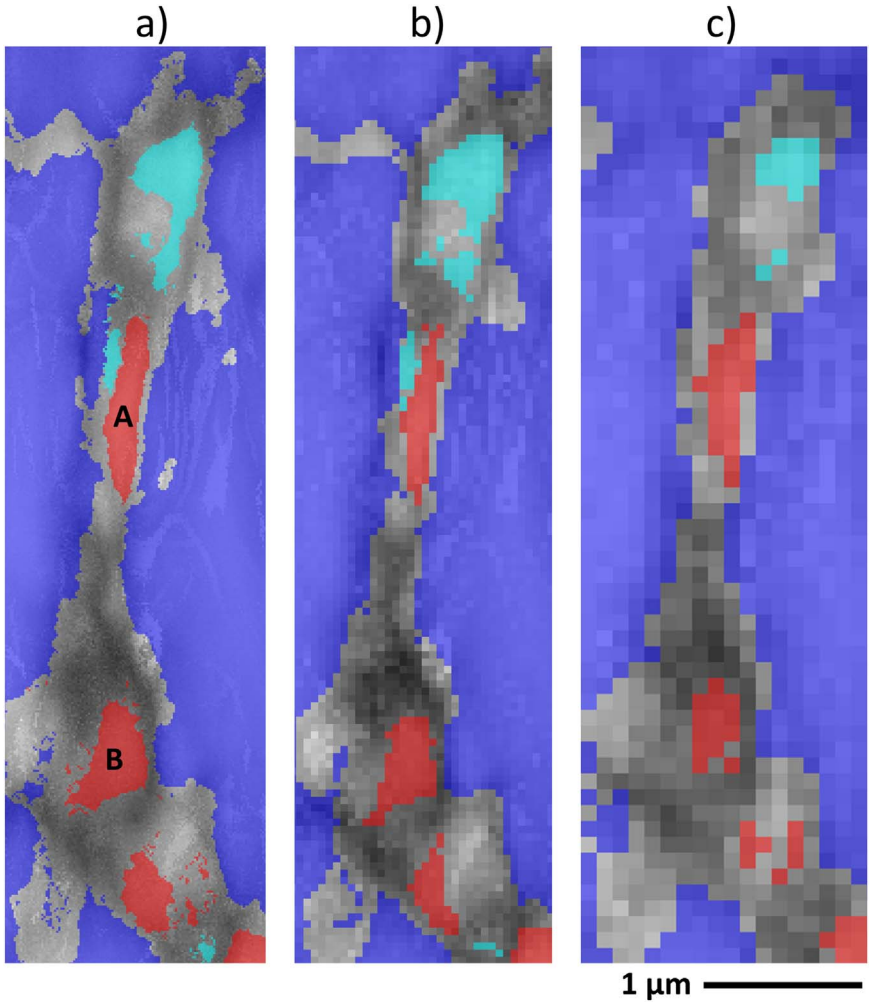

Fig. 8. Phase maps obtained from EBSD data acquired at (a) 0.014 µm, (b) 0.050 µm, and (c) 0.100 µm step sizes for the sample studied in this work. Colours corresponds to: austenite (blue); ferrite (light blue), and sigma (red). (For interpretation of the references to color in this figure legend, the reader is referred to the web version of this article.)

Table 2
Grain areas in μm^2 corresponding to the A and B grains of the σ-phases shown in Fig. 8 for different step sizes. Δ_{step} and Δ_{res} are the area uncertainties associated to the step size and transversal resolution found above, respectively.

Step (µm)	Grain					
	A			B		
	Area	Δ_{step}	Δ_{res}	Area	Δ_{step}	Δ_{res}
0.014	0.20	0.01	0.04	0.22	0.01	0.05
0.050	0.18	0.04	0.04	0.20	0.04	0.04
0.100	0.23	0.09	0.05	0.14	0.07	0.04

intermetallic FeCr compound with tetragonal $P4_2/mnm$ space group. The strategy followed to search for the presence of this phase was chosen in order to optimize the measuring time, and therefore low magnification maps (1500X) were acquired with step sizes of 0.1 or 0.2 µm. When one or more pixels were associated with the σ-phase, a new map was recorded with a higher magnification (3000X), changing also to 0.05 µm steps with the aim of analysing in more detail the size and orientation of the phase in the corresponding region. In order to set the optimal step for these high magnification images, some σ grains were analysed in maps acquired with different steps. Fig. 8 shows an example for 0.014, 0.050 and 0.100 µm steps. Although the map with the smallest step apparently looks better, it must be taken into account that the 50 nm average transversal resolution found makes many of these grains indistinguishable, as exemplified in Table 2. Since the main goal is to provide areas representative of the σ-phase and its orientations in a reasonable measurement time, a 0.050 µm step is the best alternative, as chosen in the present work.

In the sample studied, along a 37,700 µm² total scanned area, the software was able to identify 21 grains corresponding to the σ-phase, whose areas run from 0.006 μm^2 to 1.73 μm^2, amounting a total volume fraction of 0.07%. In Fig. 9, an example for the maps acquired in this sample is shown. By fitting ellipses to the identified grains, only 3 of them are found to bear characteristic dimensions below 130 nm, which can be taken as a reasonable minimum, since this is barely greater than twice the mean transversal resolution found. Despite the apparently insufficient statistics, it can be seen that the orientation of the σ-phase satisfies the relation: $\{111\}_\gamma // \{001\}_\sigma$ and $<011>_\gamma // <140>_\sigma$ (see Fig. 9), which was also observed by Lewis [41] and Weiss and Stickler [42].

5. Conclusions

The strategy followed to obtain lateral, longitudinal and depth resolutions by Monte Carlo simulations in steel allowed to estimate values of 20 nm, 75 nm, and 16 nm, respectively. The BE

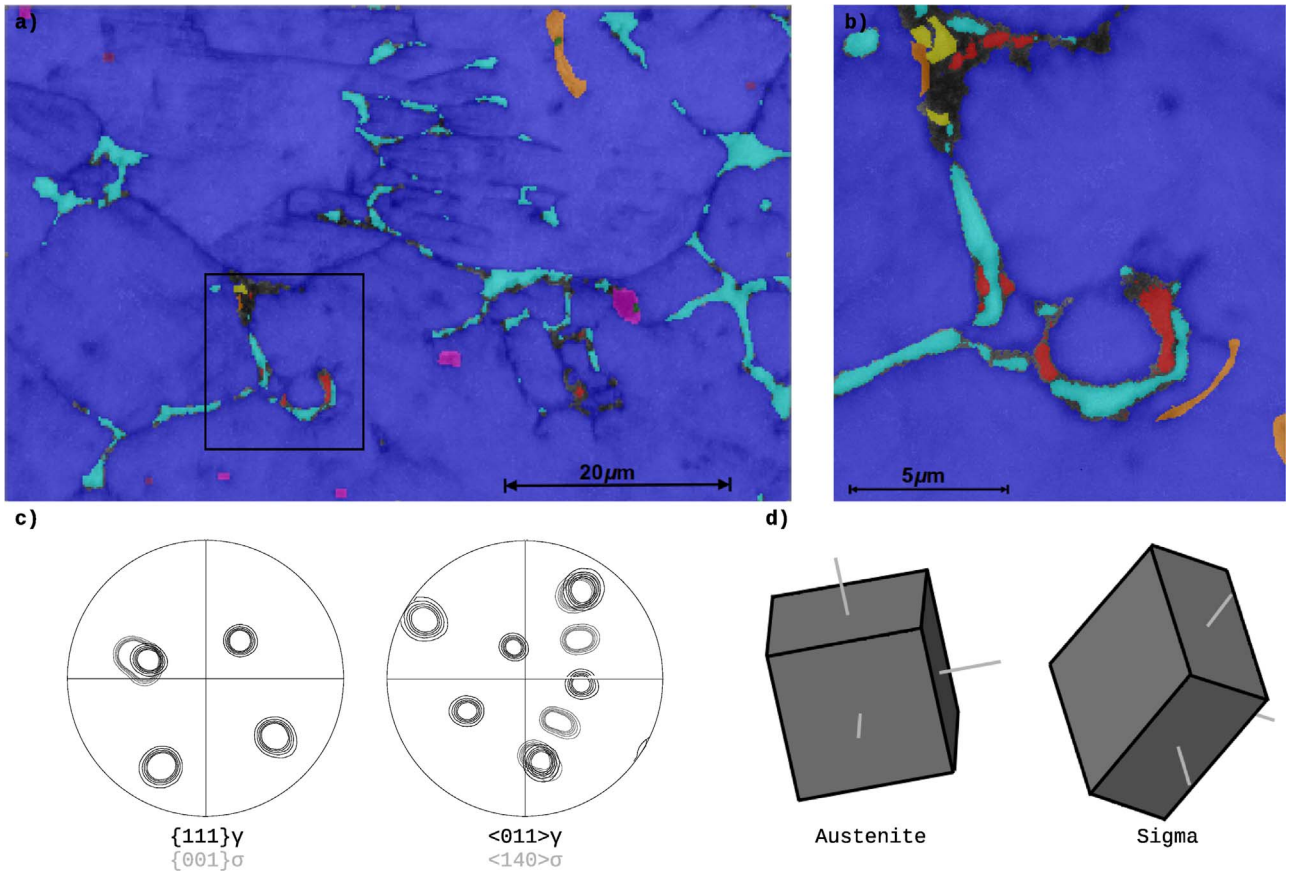

Fig. 9. Phase map obtained from EBSD data for the austenitic steel sample studied in this work with step sizes of 0.2 μm (a) and 0.05 μm (b). Colours corresponds to austenite (blue); ferrite (light blue); silicates (magenta); sulfides (green); niobium carbide (orange), sigma (red) and chromium carbide (yellow). Pole figures corresponding to the planes $\{111\}_\gamma//\{001\}_\sigma$ and to the directions $<011>_\gamma//<140>_\sigma$ are shown in (c). The corresponding orientation of the crystal units is shown in (d). (For interpretation of the references to color in this figure legend, the reader is referred to the web version of this article).

spatial distribution does not correspond to the maximum penetration distribution; on the contrary, since the outgoing electrons must not undergo additional scattering events and lose coherence, the Monte Carlo simulations carried out in this work survey the spatial coordinates where the BE last large-angle deflection occurs. Transversal resolutions are in good agreement with results obtained by other authors, whereas for the depth resolution a large dispersion can be found among the few values available in the literature.

The transversal mean resolution obtained allowed to establish a 0.05 μm step size for the EBSD maps as the best strategy for optimizing measurement times with good quality images in the particular FE-SEM used.

Low amounts of σ-phase were detected for the austenitic stainless steel under the post welding and aging heat treatments applied. This phase was observed in the ferrite-austenite interphases with an orientation relation given by: $\{111\}_\gamma//\{001\}_\sigma$ and $<011>_\gamma//<140>_\sigma$. In view of the transversal resolution achieved, the smallest grains detected were unambiguously indexed, and bear characteristic dimensions as low as 130 nm.

Acknowledgments

This work was partially supported by the *Secretaría de Ciencia y Técnica* of the *Universidad Nacional de Córdoba*, Argentina. The authors acknowledge the *Laboratorio de Microscopía Electrónica y Microanálisis* (LAMARX) of the *Universidad Nacional de Córdoba*, Argentina, where all measurements were carried out.

References

[1] D. Stojakovic, Electron backscatter diffraction in materials characterization, Process. Appl. Ceram. 6 (2012) 1–13.
[2] D. Chen, J. Kuo, W. Wu, Effect of microscopic parameters on EBSD spatial resolution, Ultramicroscopy 111 (2011) 1488–1494.
[3] F.J. Humphreys, Grain and subgrain characterisation by electron backscatter diffraction, J. Mater. Sci. 36 (2001) 3833–3854.
[4] F.J. Humphreys, Y. Huang, I. Brough, C. Harris, Electron backscatter diffraction of grain and sub-grain structures –resolution considerations, J. Microsc. 195 (1999) 212–216.
[5] D.R. Steinmetz, S. Zaefferer, Towards ultrahigh resolution EBSD by low accelerating voltage, Mater. Sci. Technol. 26 (2010) 640–645.
[6] D. Dingley, Progressive steps in the development of electron backscatter diffraction and orientation imaging microscopy, J. Microsc. 213 (2004) 214–224.
[7] S. Zaefferer, On the formation mechanisms, spatial resolution and intensity of backscatter Kikuchi patterns, Ultramicroscopy 107 (2007) 254–266.
[8] X.S. Ren, E.A. Kenik, K.B. Alexander, A. Goyal, Exploring spatial resolution in electron back-scattered diffraction experiments via Monte Carlo simulation, Microsc. Microanal. 4 (1998) 15–22.
[9] A. Deal, T. Hooghan, A. Eades, Energy-filtered electron backscatter diffraction, Ultramicroscopy 108 (2008) 116–125.
[10] A. Winkelmann, M. Vos, The role of localized recoil in the formation of Kikuchi patterns, Ultramicroscopy 125 (2013) 66–71.
[11] A. Winkelmann, M. Vos, G. Nolze, Element-specific Kikuchi patterns of Rutile, Ultramicroscopy 156 (2015) 50–58.
[12] A. Winkelmann, Principles of depth-resolved Kikuchi pattern simulation for electron backscatter diffraction, J. Microsc. 239 (2010) 32–45.
[13] M.R. Went, A. Winkelmann, M. Vos, Quantitative measurements of Kikuchi bands in diffraction patterns of backscattered electrons using an electrostatic analyzer, Ultramicroscopy 109 (2009) 1211–1216.
[14] A. Winkelmann, M. Vos, Site-specific recoil diffraction of backscattered electrons in crystals, Phys. Rev. Lett. 106 (2011) 085503.
[15] M. Vos, A. Winkelmann, Two-dimensional Kikuchi patterns of Si as measured using an electrostatic analyser, Ultramicroscopy 171 (2016) 19–25.
[16] J.M. Vitek, S.A. David, The sigma phase transformation in austenitic stainless steels, Weld. J. 65 (1986) 106–112.
[17] F. Salvat, J.M. Fernández Varea, J. Sempau, PENELOPE-2011: A code system for

Monte Carlo simulation of electron and photon transport, OECD Nuclear Energy Agency, Issy-les-Moulineaux, France, 2011.
[18] E. Acosta, E. Coleoni, G. Castellano, J.A. Riveros, J.M. Fernández-Varea, F. Salvat, Monte Carlo simulation of electron backscattering in solids using a general-purpose computer code, Scanning Microsc. 10 (1996) 625–638.
[19] C.H. Jackman, R.H. Garvey, A.E.S. Green, Yield spectra and the continuous-slowing-down approximation, J. Phys. B: At. Mol. Phys. 10 (1977) 2873–2882.
[20] F. Salvat, J. Parellada, Penetration and energy loss of fast electrons through matter, J. Phys. D: Appl. Phys. 17 (1984) 1545–1561.
[21] F. Salvat, J.M. Fernández-Varea, Overview of physical interaction models for photon and electron transport used in Monte Carlo codes, Metrologia 46 (2009) S112–S138.
[22] V. Tong, J. Jiang, A.J. Wilkinson, T.B. Britton, The effect of pattern overlap on the accuracy of high resolution electron backscatter diffraction measurements, Ultramicroscopy 155 (2015) 62–73.
[23] S.I. Wright, M.M. Nowell, R. de Kloe, L. Chan, Orientation precision of electron backscatter diffraction measurements near grain boundaries, Microsc. Microanal. 20 (2014) 852–863.
[24] M.S. Bronsgeest, J.E. Barth, L.W. Swanson, P. Kruit, Probe current, probe size, and the practical brightness for probe forming systems, J. Vac. Sci. Technol. B 26 (2008) 949–955.
[25] A. Goldenshtein, Y.I. Gold, H. Chayet, Measuring the size and intensity distribution of SEM beam spot, Proc. SPIE 3332 Metrology, Inspection, and Process Control for Microlithography XII, 132-137.
[26] L. Reimer, Scanning electron microscopy. physics of image formation and microanalysis, in: P.W. Hawkes (Ed.), 2nd. ed.,Springer Series in Optical Sciences, 45, Springer-Verlag, Berlin Heidelberg, 1998.
[27] S. Vespucci, A. Winkelmann, G. Naresh-Kumar, K.P. Mingard, D. Maneuski, P. R. Edwards, A.P. Day, V. O'Shea, C. Trager-Cowan, Digital direct electron imaging of energy-filtered electron backscatter diffraction patterns, Phys. Rev. B 92 (2015) 205301.
[28] A. Winkelmann, K. Aizel, M. Vos, Electron energy loss and diffraction of backscattered electrons from silicon, New J. Phys. 12 (2010) 053001.
[29] D.E. Newbury, Advanced scanning electron microscopy and X-ray microanalysis, Springer Science-Business Media, 1986.
[30] A. Weidenr, H. Biermann, Case studies on the application of high-resolution electron channelling contrast imaging – investigation of defects and defect arrangements in metallic materials, Philos. Mag. 95 (2015) 759–793.
[31] M. Schwind, J. Kallqvist, J.O. Nilsson, J. Agreen, H.O. Andrén, σ-phase precipitation, Acta Mater. 48 (2000) 2473–2481.
[32] Y. Minami, H. Kimura, Y. Ihara, Microstructural changes in austenitic stainless steels during long-term aging, Mater. Sci. Technol. 2 (1986) 795–806.
[33] A. Gharehbaghi, Precipitation Study in a High Temperature Austenitic Stainless Steel using Low Voltage Energy Dispersive X-ray Spectroscopy (Master Degree Thesis), School of Industrial Engineering and Management Department of Materials Science and Engineering. Royal Institute of Technology, Sweden, 2012.
[34] J. Barcik, Mechanism of σ-phase precipitation in Cr-Ni austenitic steels, Mater. Sci. Technol. 4 (1988) 5–15.
[35] D.M.E. Villanueva, F.C.P. Junior, R.L. Plaut, A.F. Padilha, Comparative study on sigma phase precipitation of three types of stainless steels: austenitic, superferritic and duplex, Mater. Sci. Technol. 22 (2006) 1098–1104.
[36] V.K. Sikka, M.G. Cowgill, B.W. Roberts, Creep properties of modified 9Cr-Mo steel, Proceedings of topical conference on ferritic alloys for use in nuclear energy technologies. ASM International 1983.
[37] E.J. Chun, H. Baha, K. Terashima, K. Nishimoto, K. Saida, Prediction of σ phase precipitation in type 316FR stainless steel weld metal, Weld. Soc. Proc. 31 (2013) 168–172.
[38] Y.S. Na, N.Y. Park, R.C. Reed, Sigma morphology and precipitation mechanism in Udimet 720Li, Scr. Mater. 43 (2000) 585–590.
[39] L.K. Singhal, J.W. Martin, The formation of ferrite and sigma phase in some austenitc stainless steels, Acta Metall. Mater. 16 (1968) 1441–1451.
[40] H.L. Jr Yakel, Atom distribution in sigma-phases. I. Fe and Cr distribution in a binary phase equilibrated at 1063, 1013 and 923 K, Acta Cryst. B 39 (1983) 20–28.
[41] M.H. Lewis, Precipitations of (Fe,Cr) σ phase from austenite, Acta Metall. Mater. 14 (1966) 1421–1428.
[42] B. Weiss B, R. Stickler, Phase instabilities during high temperature exposure of 316 austenitic stainless steel, Metall. Mater. Trans. A 3 (1972) 851–866.